

REPORT DOCUMENTATION PAGE				Form Approved OMB No. 0704-0188	
Public reporting burden for this collection of information is estimated to average 1 hour per response, including the time for reviewing instructions, searching existing data sources, gathering and maintaining the data needed, and completing and reviewing this collection of information. Send comments regarding this burden estimate or any other aspect of this collection of information, including suggestions for reducing this burden to Department of Defense, Washington Headquarters Services, Directorate for Information Operations and Reports (0704-0188), 1215 Jefferson Davis Highway, Suite 1204, Arlington, VA 22202-4302. Respondents should be aware that notwithstanding any other provision of law, no person shall be subject to any penalty for failing to comply with a collection of information if it does not display a currently valid OMB control number. PLEASE DO NOT RETURN YOUR FORM TO THE ABOVE ADDRESS.					
1. REPORT DATE (DD-MM-YYYY) May 1, 2007		2. REPORT TYPE Final Report		3. DATES COVERED (From - To) 11/01/2003-01/31/2007	
4. TITLE AND SUBTITLE Gravity-Wave Dynamics in the Atmosphere				5a. CONTRACT NUMBER	
				5b. GRANT NUMBER FA9950-04-1-0125	
				5c. PROGRAM ELEMENT NUMBER	
6. AUTHOR(S) Akylas, Triantaphyllos, R.				5d. PROJECT NUMBER	
				5e. TASK NUMBER	
				5f. WORK UNIT NUMBER	
7. PERFORMING ORGANIZATION NAME(S) AND ADDRESS(ES) Massachusetts Institute of Technology 77 Massachusetts Avenue Cambridge, MA 02139				20070516074	
9. SPONSORING / MONITORING AGENCY NAME(S) AND ADDRESS(ES) Air Force Office of Scientific Research Dr. Arje Nachman-NE 875 North Randolph Road Ste. 325, Room 3112 Arlington, VA 22203				10. SPONSOR/MONITOR'S ACRONYM(S)	
				11. SPONSOR/MONITOR'S REPORT NUMBER(S)	
12. DISTRIBUTION / AVAILABILITY STATEMENT <i>Distribution Statement A: unlimited</i> AFRL-SR-AR-TR-07-0149					
13. SUPPLEMENTARY NOTES					
14. ABSTRACT The flow of wind over mountain ranges is believed to be one of the primary generation mechanisms of atmospheric gravity waves. Mountain gravity waves contribute to the production of stratospheric turbulence, a potential cause of accidents in high-altitude aircraft flights. In an effort to advance the current capabilities of forecasting stratospheric turbulence, theoretical models have been developed for the generation and breakdown of mountain gravity waves under realistic conditions, including effects not captured by existing forecasting tools. Specifically, short-scale oscillations in the background buoyancy-frequency profile, often seen in balloon measurements, but normally ignored in theoretical models, are found to cause significantly increased gravity-wave activity, resulting in wave breaking above and upstream of the mountain. The effect of temporal variations in the wind velocity is also studied for a range of amplitudes and periods typical of those encountered in the field. Transient gravity waves resulting from such variations can be significant, and steady flow states predicted on the assumption of uniform wind may not be attainable. Finally, a study is made of the nonlinear evolution of a gravity-wave packet as it propagates upwards in the atmosphere, generating low-frequency inertial-gravity waves of the type seen in recent field observations.					
15. SUBJECT TERMS					
16. SECURITY CLASSIFICATION OF:			17. LIMITATION OF ABSTRACT	18. NUMBER OF PAGES	19a. NAME OF RESPONSIBLE PERSON
a. REPORT	b. ABSTRACT	c. THIS PAGE			19b. TELEPHONE NUMBER (include area code)

I. EXECUTIVE SUMMARY

The main objectives of this project were: to advance the understanding of the generation, propagation and breakdown of atmospheric gravity waves owing to mountains; to develop improved theoretical models for forecasting stratospheric gravity waves under realistic flow conditions; and to examine the role of gravity waves in the production of turbulence under various flow conditions.

Towards reaching these goals, the following specific problems have been studied:

(i) As indicated by balloon measurements, atmospheric buoyancy profiles, apart from a sharp increase (roughly by a factor of 2) at the tropopause, often feature appreciable oscillations (typical wave length 1–2 km) with altitude. Based on numerical solutions of the Euler equations, we find that such short-scale oscillatory variations of the background buoyancy frequency, which usually are ignored in theoretical models, can have a profound effect on the generation of mountain waves owing to a resonance mechanism that comes into play at certain wind speeds depending on the dominant oscillation wave length. As suggested by our earlier asymptotic results for small-amplitude sinusoidal oscillations, comprehensive numerical studies for more realistic flow conditions confirm that, under resonant conditions, the induced gravity-wave activity is significantly increased, often resulting in wave breaking above and upstream of the mountain, similarly to resonant flow of finite depth over topography. This piece of work forms part of the doctoral thesis of I. Skopovi (completed, May 2006). For technical details, see Sec. A below.

(ii) The effects of unsteadiness in the wind have received relatively little attention in prior studies of mountain gravity waves. To fill this gap, the effect of temporal variations in the wind velocity was studied. Motivated by field observations, which typically exhibit strong oscillatory fluctuations about a steady mean, we considered the case of a time-harmonic component superposed on a constant wind. We find that, for relatively short (on the order of min.) wind fluctuations, the unsteady wind component can be safely averaged out. On the other hand, for larger-period (hours or days) fluctuations, the effect of unsteadiness is very significant. In particular, steady flow states, predicted on the assumption of uniform wind, may not be attainable owing to transient wave breaking. This forms the second part of I. Skopovi's doctoral thesis (May 2006). For technical details, see Sec. B below.

(iii) Recent balloon measurements in the course of the French gravity wave campaign indicate that low-frequency (hydrostatic) gravity waves are ubiquitous in the atmosphere. These are large-scale disturbances (horizontal length of hundreds of km) for which the effects of the Earth's rotation cannot be neglected. In an effort to understand how energy gets transferred to such low-frequency motions, we studied the nonlinear evolution of a non-hydrostatic wave-train as it propagates upwards in the atmosphere. We find that the envelope of the wavetrain

can interact resonantly with low-frequency gravity–inertial wave modes. This resonant interaction causes radiation of energy away from the gravity wavetrain, forming a trailing wake of gravity–inertial waves. Moreover, the gravity wavetrain may experience rapid wavenumber variations in certain locations, where eventually caustics form, signaling the onset of a breakdown process. This is joint work with Dr. Ali Tabaei, who was supported by the grant as a post-doctoral research associate. Technical details can be found in a forthcoming article in *Studies in Applied Mathematics* (Tabaei & Akylas 2007).

– Personnel supported

Professor T.R. Akylas, Dr. A. Tabaei (post-doctoral Research Associate), I. Skopovi (graduate Research Assistant)

– Publications

Skopovi, I. & Akylas, T.R., “The Role of Buoyancy-Frequency Oscillations in the Generation of Mountain Gravity Waves”, *Theoretical and Computational Fluid Dynamics*, in press.

Skopovi, I. & Akylas, T.R., “Effects of Temporal Variations in Wind Velocity on the Generation of Mountain Gravity Waves”, *Theoretical and Computational Fluid Dynamics*, to be submitted.

Tabaei, A. & Akylas, T.R., “Resonant Long–Short Wave Interactions in an Unbounded Rotating Stratified Fluid”, *Studies in Applied Mathematics*, in press.

Akylas, T.R., “Solitary Waves in Rotating Fluids”, Chapter 5 in *Solitary Waves in Fluids* (ed. R.H.J. Grimshaw) WIT Press 2007.

Akylas, T.R., Grimshaw, R.H.J., Clarke, S.R. & Tabaei, A., “Reflecting Tidal Wave Beams and Local Generation of Solitary Waves in the Ocean Thermocline”, *Journal of Fluid Mechanics*, under review.

Skopovi, I., “The Role of Background Flow Variations in Stratified Flows Over Topography”, PhD Thesis, May 2006.

II. TECHNICAL DESCRIPTION

A. Effects of Buoyancy-Frequency Oscillation on the Generation of Mountain Waves

The flow of wind over mountain ranges is believed to be one of the primary generation mechanisms of gravity waves in the atmosphere. Typically, mountain waves develop instabilities as they propagate upwards in the atmosphere and eventually breakdown into turbulence. There is now increasing evidence (Eckermann and Preusse [11]) that breaking mountain waves in fact contribute significantly to turbulence activity in the upper troposphere and lower stratosphere, at altitudes 10–15 km, and several accidents in high-altitude aircraft flights have been attributed to unexpected mountain-wave-induced stratospheric turbulence (Eckermann et al. [10]).

From a theoretical point of view, the generation of internal gravity waves by stratified flow over topography is a classical problem of fluid dynamics. Early work used linear models to study the formation of two-dimensional disturbances on the lee side of the topography – the so-called lee-wave problem – under perfectly uniform background flow conditions (constant wind-velocity and buoyancy-frequency profiles). For these idealized flow conditions, and on the further assumption of steady flow, there is also a nonlinear analytical model (Long [17]) that has been used to explore wave breaking of two-dimensional disturbances over finite-amplitude topography (see Baines [1] for a comprehensive review).

In the atmosphere, however, the buoyancy frequency and the wind speed are far from uniform. Typical profiles, from balloon measurements in the lee of Mt. Washington, are shown in Fig. 1. The mean profiles vary significantly with altitude near the tropopause, the borderline between the troposphere and the stratosphere. In this instance, the tropopause is at about 12 km from the ground and the mean buoyancy frequency increases by roughly a factor of 2 there. In addition, the buoyancy-frequency profile and to a lesser extent the wind speed exhibit appreciable fluctuations on a lengthscale of 1–2 km about their mean values.

In more recent theoretical work, attempts have been made to account for the effect of non-uniform background buoyancy frequency. Extending Long's model, Durran [9] studied nonlinear steady-state hydrostatic disturbances over finite-amplitude topography for buoyancy-frequency profiles with two layers of uniform stratification, the interface modeling the tropopause. Depending on the height at which the buoyancy-frequency jump is positioned, the streamline deflections can be maximized/minimized over the topography, thus enhancing/suppressing wave breaking in comparison with the predictions of Long's model. This tuning/detuning effect persists for continuous buoyancy-frequency profiles with a smooth transition at the tropopause, as demonstrated by Davis [8].

For the purpose of forecasting mountain waves in the field, Eckermann and co-workers [7] recently devised a hybrid methodology, combining linear theory to estimate the near-field response close to the topography, with a ray-tracing technique that accounts for gradual variations of the buoyancy frequency and wind speed in the far field.

In the present work, we study a model of stratified flow over topography that accounts for the tropopause as well as possible oscillatory variations of the background buoyancy fre-

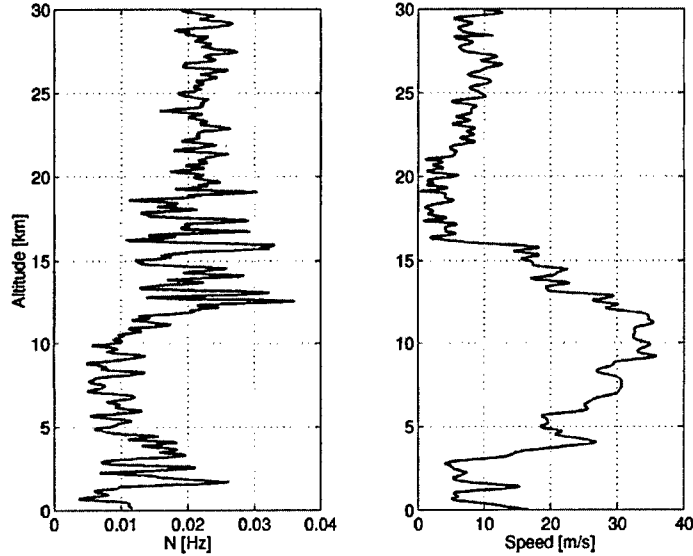


Fig. 1 Balloon measurements in the lee of Mt. Washington (a) buoyancy frequency, and (b) flow speed as a function of altitude (courtesy of Dr. R. Beland).

quency. The potential significance of the latter was pointed out in Prasad and Akylas [20] using an asymptotic theory for stratified flow with constant mean buoyancy frequency near the hydrostatic limit. Under these special flow conditions, the presence of small sinusoidal variations in the buoyancy frequency can have a dramatic effect owing to a resonance mechanism brought about by the coupling of the internal gravity waves with the background flow variations. As suggested by Phillips [19], this wave-background-flow interaction causes trapping of the disturbance close to the topography; as a result, near certain critical flow speeds, the response behaves similarly to resonant flow of finite depth, exhibiting significantly increased gravity-wave activity over the topography as well as upstream influence in the form of solitary waves and bores.

Here we explore this resonance mechanism under more realistic flow conditions by solving the Euler equations using numerical methods. It turns out that periodic variations of the buoyancy frequency continue to play an important part even when the mean buoyancy profile is not constant due to the presence of the tropopause, although strictly the theory of Prasad and Akylas [20] is no longer valid. As the lengthscale of the assumed buoyancy-frequency oscillations is comparable to the vertical wavelength of the induced gravity waves, the effects of such short-scale variations cannot be captured by ray tracing.

Preliminaries

We shall use the same non-dimensional formulation as in Prasad and Akylas [20] for inviscid incompressible flow over localized topography with horizontal lengthscale L and peak amplitude H . Denoting the upstream flow speed by U_0 and by N_0 a characteristic value of the

Brunt–Väisälä (buoyancy) frequency, the flow is governed by three independent parameters

$$\mu = \frac{U_0}{N_0 L}, \quad \varepsilon = \frac{H N_0}{U_0}, \quad \beta = \frac{N_0 U_0}{g}, \quad (1)$$

g being the gravitational acceleration. The Boussinesq parameter β is a measure of stratification; the long-wave parameter μ and the amplitude parameter ε control dispersive and nonlinear effects, respectively.

Employing L and U_0/N_0 as the characteristic lengthscales along the horizontal (x -) and vertical (y -) directions, respectively, and L/U_0 as the timescale, the governing equations (in the Boussinesq limit, $\beta \rightarrow 0$) for the velocity field $\mathbf{u} = (u, \mu v)$, and the perturbations of density $\beta \rho$ and pressure p from hydrostatic equilibrium, are

$$\nabla \cdot \mathbf{u} = 0, \quad (2)$$

$$\rho_t + \mathbf{u} \cdot \nabla \rho - N^2 v = 0, \quad (3)$$

$$\mathbf{u}_t + \mathbf{u} \cdot \nabla \mathbf{u} = - (p_x, \mu^{-2}(\rho + p_y)). \quad (4)$$

Here $N(y)$ denotes the background Brunt–Väisälä frequency, defined by

$$\bar{\rho}_y = -\beta \bar{\rho} N^2, \quad (5)$$

in terms of the background density $\bar{\rho}(y)$. Moreover, the boundary condition on the topography $y = \varepsilon h(x)$ reads

$$v = \varepsilon u \frac{dh}{dx} \quad (y = \varepsilon h). \quad (6)$$

In the present study, it will be assumed that the Brunt–Väisälä frequency consists of a mean profile with oscillations superposed on it. Denoting by λ the typical lengthscale of the oscillations, this introduces an additional parameter which we take to be

$$F = \frac{U_0 \pi}{\lambda N_0}. \quad (7)$$

In Prasad and Akylas [20], the parameter F plays the role of a Froude number as it defines the critical-flow regime in which resonance occurs, in analogy with resonant flow over topography in a channel of finite depth (Grimshaw and Smyth [13], Grimshaw and Yi [12]).

Specifically, the theory of Prasad and Akylas [20] applies to the nearly hydrostatic response ($\mu \ll 1$) in the case that small sinusoidal oscillations of wavelength λ are superposed on a uniform mean buoyancy profile:

$$N^2(y) = 1 + \mu^2 \{q_1 \sin(2Fy) + q_2 \cos(2Fy)\}. \quad (8)$$

For this choice of N , the background flow is nearly uniformly stratified and, according to Long's model, the steady-state response, to leading order in μ , is a columnar sinusoidal disturbance with wavelength equal to 2π in the vertical direction; the weak background-flow variations in (8), small deviations from the hydrostatic limit, and unsteady-evolution effects

merely modulate this columnar disturbance. Accordingly, the perturbation streamfunction ψ , in terms of which $u = 1 + \psi_y$, $v = -\psi_x$, is posed as

$$\psi = \{A(x, Y, T)e^{iy} + cc\} + O(\mu^2), \quad (9)$$

where cc denotes the complex conjugate, and the asymptotic theory furnishes an evolution equation for the complex envelope A of the columnar disturbance as a function of the stream-wise coordinate x , the ‘stretched’ vertical coordinate $Y = \mu^2 y$ and the ‘slow’ time $T = \mu^2 t$.

From Phillips [19], resonance is expected to occur when the wavelength of the background-flow variations is about one half of the response wavelength, so $F \approx 1$. Setting then

$$F = 1 + \sigma\mu^2, \quad (10)$$

$\sigma = O(1)$ being a resonance detuning parameter, it follows that the linear ($\varepsilon \ll 1$) hydrostatic response is governed by the evolution equation

$$A_T - iA_{xY} - \frac{1}{4}e^{2i\sigma Y}QA_x^* = 0, \quad (11)$$

where A^* is the complex conjugate of A and $Q = q_2 - iq_1$; the last term of this equation accounts for the coupling of the induced columnar disturbance with the mean-flow variations. In addition, from (6) and (9), the linearized boundary condition on the topography is

$$a = -\frac{\varepsilon}{2}h(x) \quad (Y = 0), \quad (12)$$

where a is the real part of A .

The critical Froude number at which resonance occurs can be found by solving equation (11) subject to (27) for the steady-state linear hydrostatic response. To this end, we write

$$A = \hat{A}e^{i\sigma Y} \quad (13)$$

so that, upon substitution into (11), \hat{A} satisfies an evolution equation with constant coefficients. The steady version of this equation corresponds to the following equation system

$$\sigma\hat{a} + \hat{b}_Y - \frac{1}{4}q_2\hat{a} + \frac{1}{4}q_1\hat{b} = 0, \quad (14a)$$

$$\sigma\hat{b} - \hat{a}_Y + \frac{1}{4}q_1\hat{a} + \frac{1}{4}q_2\hat{b} = 0 \quad (14b)$$

in terms of the real and imaginary parts of $\hat{A} = \hat{a} + i\hat{b}$. Moreover, \hat{a} must satisfy the boundary condition (27). The solution is found to be

$$\hat{a} = -\frac{\varepsilon}{2}h(x)e^{-sY}, \quad \hat{b} = \frac{\varepsilon}{2}h(x)\frac{q_1 + 4s}{q_2 + 4\sigma}e^{-sY}, \quad (15)$$

where

$$s^2 = -\sigma^2 + \frac{1}{16}(q_1^2 + q_2^2). \quad (16)$$

From (15) and (16), it is clear that the steady-state response becomes singular, and hence resonance occurs, when

$$\sigma = -\frac{1}{4}q_2, \quad q_1 > 0. \quad (17)$$

Combined with (10), this in turn determines the critical Froude number $F = F_{\text{crit}}$,

$$F_{\text{crit}} = 1 - \frac{1}{4}q_2\mu^2, \quad q_1 > 0 \quad (18)$$

at which the flow is resonant according to the linear hydrostatic theory.

Prasad and Akylas [20] examined the implications of this resonance based on the evolution equation satisfied by the complex envelope A – the nonlinear, weakly dispersive analogue of (11) – which is valid asymptotically when small sinusoidal variations are present on an otherwise uniform Brunt–Väisälä frequency in nearly hydrostatic nonlinear flow over topography. Here we explore the role that this resonance plays under less restricted flow conditions by solving the full Euler equations (2)–(4) numerically.

Uniform mean buoyancy-frequency profile

We have constructed a numerical model for solving the Euler equations (2)–(4) for stratified flow over topography with uniform wind speed but general buoyancy-frequency profile far upstream. Since the flow domain is unbounded, a major issue is how to avoid artificial reflections at the boundaries of the computational domain. For this purpose, the model employs absorbing viscous layers at the upper and lateral boundaries. A description of the numerical procedure along with details of implementation can be found in the Appendix.

In all our computations, we have used the algebraic topography profile, also known as ‘Witch of Agnesi’,

$$h(x) = \frac{1}{1+x^2}, \quad (19)$$

and have taken $\varepsilon = 0.6$; for uniformly stratified ($N=1$) hydrostatic flow over the topography (19), according to Long’s model, nonlinear effects come into play roughly above this value of ε which, however, is still well below the critical value of $\varepsilon = 0.85$ required for overturning (wave breaking).

Our first choice of flow conditions mimics those considered in Prasad and Akylas [20], namely the upstream buoyancy-frequency profile is given by (8) with $\mu^2 q_1 = 0.25 \cos \phi$, $\mu^2 q_2 = 0.25 \sin \phi$ ($-\pi < \phi < \pi$). (The sinusoidal oscillations are terminated at $y = 12\pi$ and above this height the buoyancy frequency is held constant at $N=1$; the numerical stratification profile thus comprises $12F$ oscillation periods, in contrast to the asymptotic theory that assumes infinitely many oscillations.) According to (18), for this choice of $\mu^2 q_1$ and $\mu^2 q_2$, resonance is possible when $-\pi/2 < \phi < \pi/2$; for any ϕ in this range, the critical Froude number then is given by

$$F_{\text{crit}} = 1 - \frac{\sin \phi}{16}. \quad (20)$$

As a first example, we take $\phi = 0$ and $F = 1$, corresponding to exact resonant conditions according to (20). Fig. 2(a) shows streamline patterns for this set of parameters and $\mu = 1/6$ at $t = 50$ and $t = 150$, while Fig. 2(b) contrasts the response at $t = 150$ against the solution we would have obtained at the same time in the absence of buoyancy-frequency oscillations far upstream; by $t = 150$, the response for constant N has essentially reached the steady state

predicted by Long's model. It is evident that the variations of the Brunt–Väisälä frequency alter the nature of the flow dramatically: the gravity-wave activity is markedly increased over the topography, the streamline peak amplitudes associated with the resonant response at $t = 150$ being nearly twice as large as those of uniformly stratified flow. In the resonant response, moreover, we see the emergence of upstream-wave propagation along with a disturbance of opposite sign forming on the downstream side of the topography. This behavior, which is characteristic of resonant flow in a channel of finite depth (Grimshaw and Smyth [13], Grimshaw and Yi [12]), was also found in Prasad and Akylas [20] and must be attributed to the trapping effect caused by the interaction of the induced disturbance with the background buoyancy-frequency oscillations. In the asymptotic theory, the response was tracked in terms of the scaled time $T = \mu^2 t$, corresponding to significantly larger values of t than those in Fig. 2; at such later times, typically, wave breaking occurs and the upstream disturbance evolves into solitary waves or bores.

Fig. 3 shows two snapshots of the response for $\mu = 0.05$, $F = 1$ and $\phi = \pi/3$ instead of $\phi = 0$. From (18), this change of the phase ϕ lowers the value of the critical Froude number to $F_{\text{crit}} = 0.957$ so $F = 1$ is supercritical under the present flow conditions. As a result, the response in Fig. 3 is quite different from that shown in Fig. 2(a): the streamline peak amplitudes are generally smaller, there is no upstream-wave propagation, and apparently steady state is approached as the transients are swept downstream. Fig. 3 also shows, for comparison, the hydrostatic steady-state response corresponding to the present flow conditions, as obtained following the numerical procedure of Davis [8]; this confirms that the unsteady response indeed reaches steady state. On the other hand, by lowering the Froude number to the critical value of $F_{\text{crit}} = 0.957$ given by (18), the response again becomes resonant (see Fig. 4). (We remark that the smaller value of $\mu = 0.05$, which is closer to the hydrostatic limit, rather than $\mu = 1/6$, was used in Fig. 3, only to facilitate comparison against the hydrostatic steady state; the difference between the resonant and non-resonant behavior is controlled by F and is not affected by this choice of μ .)

The results of fully numerical simulations reported above support the conclusions reached by the asymptotic theory of Prasad and Akylas [20]. Superposing sinusoidal variations on a uniform mean buoyancy-frequency profile indeed causes trapping of gravity wave disturbances in the vertical direction, and the flow behaves as if it were in a channel of finite depth. The response turns out to be very sensitive to small changes in the background-flow conditions and, near the critical Froude number, features increased gravity-wave activity and upstream influence. In the following section, we explore the role of this resonance mechanism when the buoyancy profile takes into account the tropopause.

Effects of the tropopause

We shall model the transition from the troposphere to the stratosphere by the dimensionless mean buoyancy-frequency profile

$$\langle N \rangle = 1.5 + 0.5 \tanh 2(y - d), \quad (21)$$

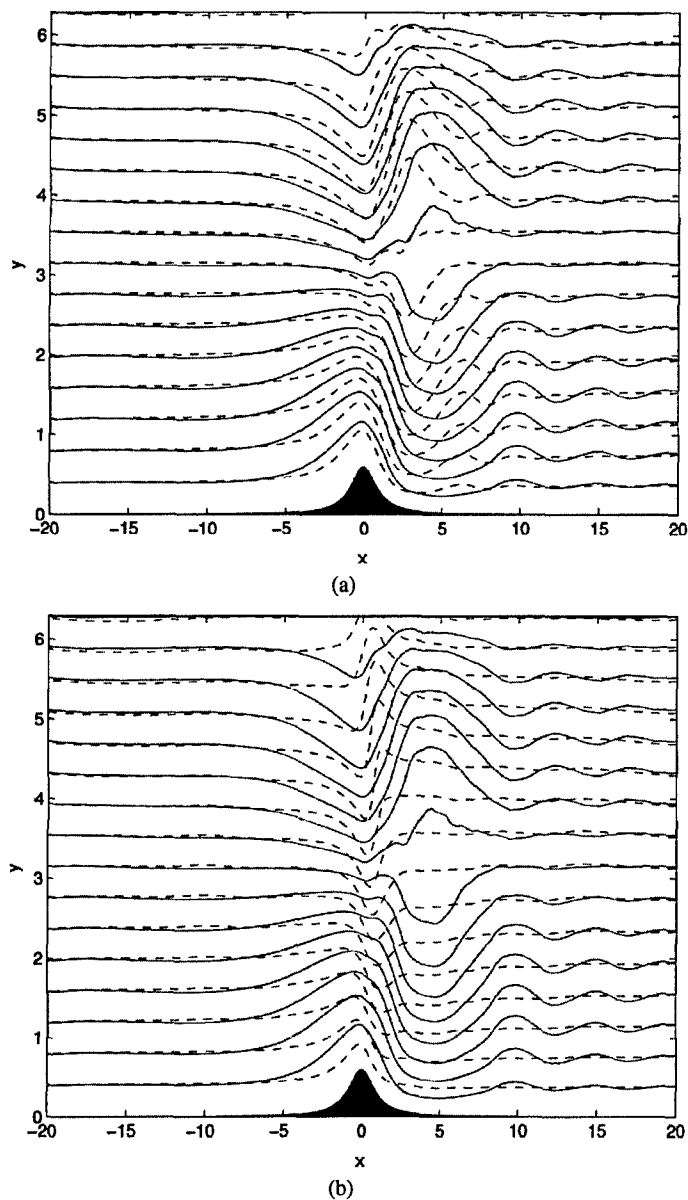


Fig. 2 Resonant response for $F=1$, $\phi=0$ and $\mu=1/6$ (a) evolution in time: dashed line $t=50$, solid line $t=150$; (b) comparison between the resonant response (solid line) and the solution for uniform buoyancy frequency profile (dashed line) at $t=150$.

where d is a parameter that controls the tropopause height. Consistent with Fig. 1(a), the profile (56) is such that $\langle N \rangle$ varies smoothly from 1 in the troposphere ($y \ll d$) to 2 in the stratosphere ($y \gg d$). Referring to Fig. 1, a typical value of the mean buoyancy frequency in the troposphere is $N_0 = 0.01 \text{sec}^{-1}$ and the wind speed is in the range 5–30 m/sec, so

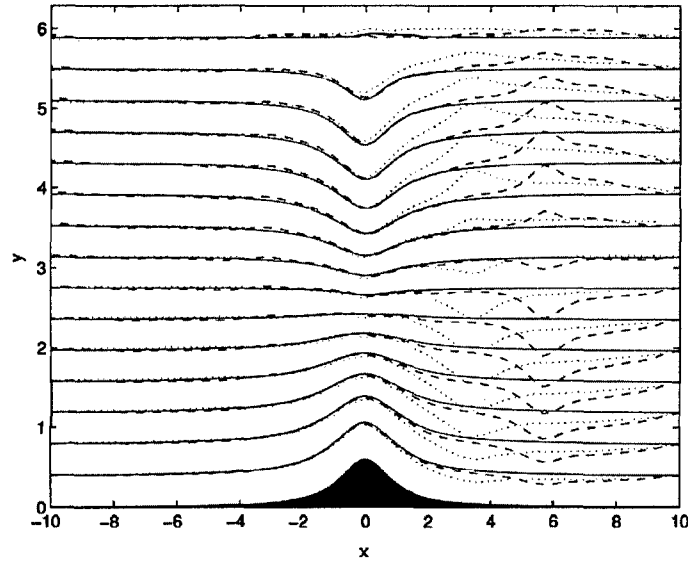


Fig. 3 Non-resonant response for $F=1$, $\phi=\pi/3$ and $\mu=0.05$ at $t=50$ (dotted line) and $t=100$ (dashed line). The corresponding hydrostatic steady-state solution (solid line) is also shown for comparison.

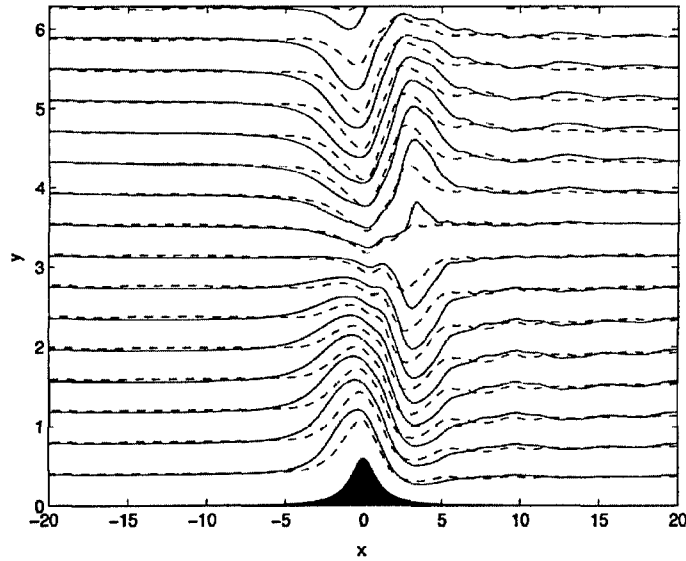


Fig. 4 Time evolution of resonant response for $F=0.957$, $\phi=\pi/3$ and $\mu=1/6$: dashed line $t=50$, solid line $t=150$.

the characteristic lengthscale $U_0/N_0 \sim 0.5 - 3$ km. Generally, the atmospheric tropopause height varies from 10 to 14 km which, in terms of the dimensionless parameter d , would then correspond to $d \sim 5-25$.

The steady-state hydrostatic response for a two-layer buoyancy-frequency profile with a finite jump at the interface of the two layers was studied by Durran [9] and later Davis [8] considered the same problem for a continuously varying buoyancy frequency as in (56). They both find specific tropopause heights for which the hydrostatic steady-state response exhibits enhanced or reduced gravity-wave activity. For $\varepsilon = 0.6$, for example, such ‘tuned’ and ‘detuned’ gravity-wave flow fields occur when the tropopause is placed in the vicinity of $d = 21$ and $d = 25$, respectively. In fact, consistent with Durran [9] and Davis [8], we find multiple ‘tuned’ and ‘detuned’ responses that recur periodically with changing d , the lowest value of d that corresponds to a ‘tuned’ response being in the neighborhood of $d = 6$.

For two-layer buoyancy-frequency profiles with sharp interface, Durran [9] and Davis [8] also noted that their numerical procedures failed to converge to a hydrostatic steady-state solution at certain tropopause heights. While Durran [9] suggested that this anomaly could indicate a nonlinear-resonance phenomenon, Davis [8] attributed the lack of convergence to numerical difficulties.

For the purpose of validating and clarifying the steady-state results of Durran [9] and Davis [8], we have carried out unsteady numerical simulations using the buoyancy-frequency profile (56) close to the hydrostatic limit ($\mu = 0.05$). We find that the unsteady response generally approaches the steady state predicted by the previous studies; a typical example is shown in Fig. 5 for $d = 3$. We also investigated the nature of the response for buoyancy profiles with sharp transition at the tropopause for the values of d at which Durran [9] and Davis [8] experienced difficulties converging to a hydrostatic steady state. Near these special values of d ($d = 4.5, 11, 17.3, 23.5, \dots$), it turns out that the steady-state response approaches the uniform stream far upstream and downstream much more slowly than Long’s solution, and a sufficiently large computational domain is required along x in order to achieve convergence (see Fig. 6). Also our numerical simulations indicate that the corresponding unsteady response tends to steady state, albeit relatively slowly, and there is no sign of a nonlinear resonance.

Next, we superpose on the mean buoyancy profile (56) sinusoidal oscillations similar to those used in (8) for the uniform mean profile:

$$N^2(y) = \{1.5 + 0.5 \tanh[2(y - d)]\}^2 + \mu^2 \{q_1 \sin(2Fy) + q_2 \cos(2Fy)\} \quad (22)$$

with $\mu^2 q_1 = 0.25 \cos \phi$, $\mu^2 q_2 = 0.25 \sin \phi$ as before. Fig. 7 shows the unsteady response for $\mu = 1/6$, $\phi = 0$ and $F = 1$ at $t = 50$ and $t = 150$ when the tropopause is placed at $d = 21$. Note that, for uniform mean buoyancy frequency equal to 1, this choice of flow parameters would correspond to resonant conditions in the troposphere ($y \ll d$) according to (20), but for the buoyancy-frequency profile (22), which includes the tropopause, strictly the resonance equation (20) is no longer valid. Nevertheless, upon comparing Fig. 7 with Fig. 2, the salient features of resonant response identified earlier – increased wave amplitudes over the topography and upstream-wave formation – are still present, suggesting that the resonance mechanism persists when the tropopause is taken into account; even when trapping occurs in the troposphere only, resonance is still possible. Finally, Fig. 8 shows the response for the

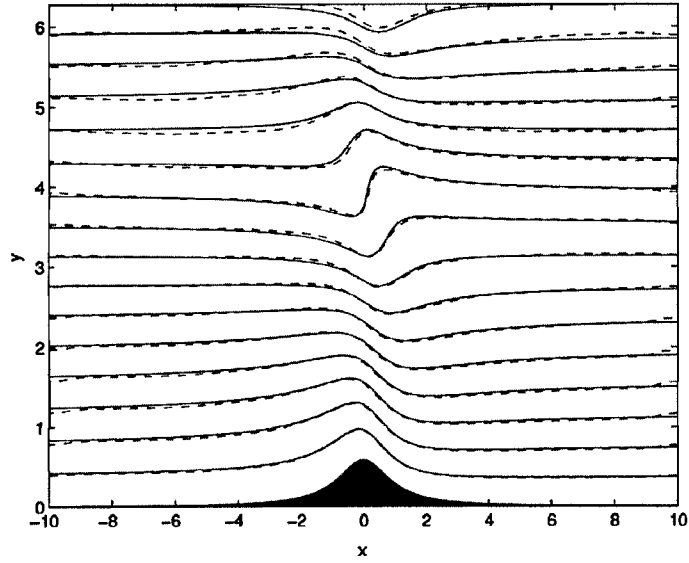


Fig. 5 Comparison of the response for tropopause height $d=3$ and $\mu=0.05$ at $t=50$ (dashed line) with the corresponding hydrostatic steady-state solution (solid line). At this time, steady state has essentially been reached below $y=3$.

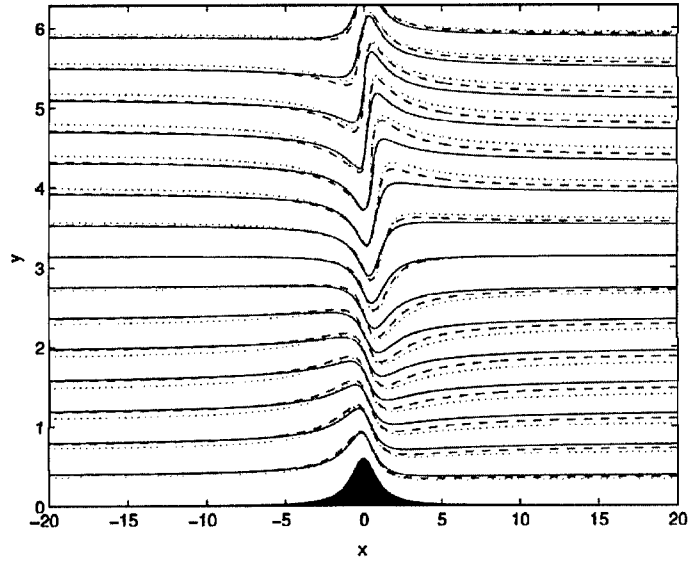


Fig. 6 Contrast between Long's solution (solid line) and the steady-state hydrostatic response for $d=23.25$ computed using a domain of width $x=\pm 50$ (dotted line) and $x=\pm 100$ (dashed line).

same flow parameters as in Fig. 7 but with $\phi = \pi/3$. As expected, this response is not resonant and approaches steady state as the non-resonant case shown in Fig. 3.

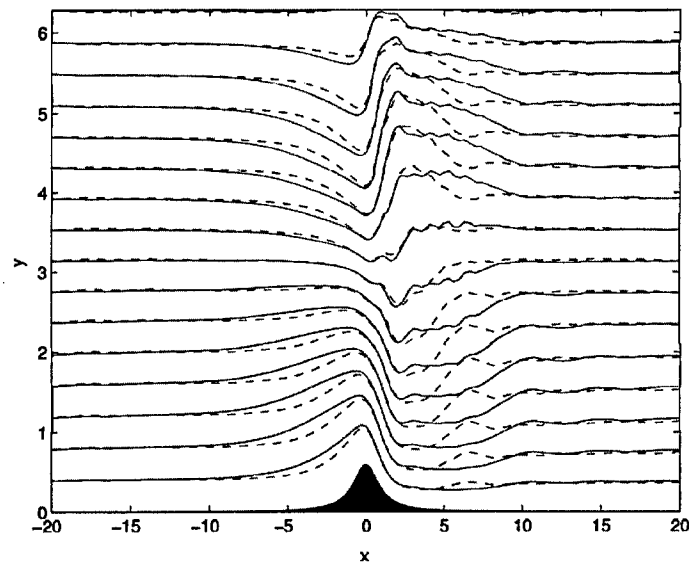


Fig. 7 Time evolution of resonant response for $F=1$, $\phi=0$ and $\mu=1/6$ in the presence of a tropopause at $d=21$: dashed line $t=50$, solid line $t=150$.

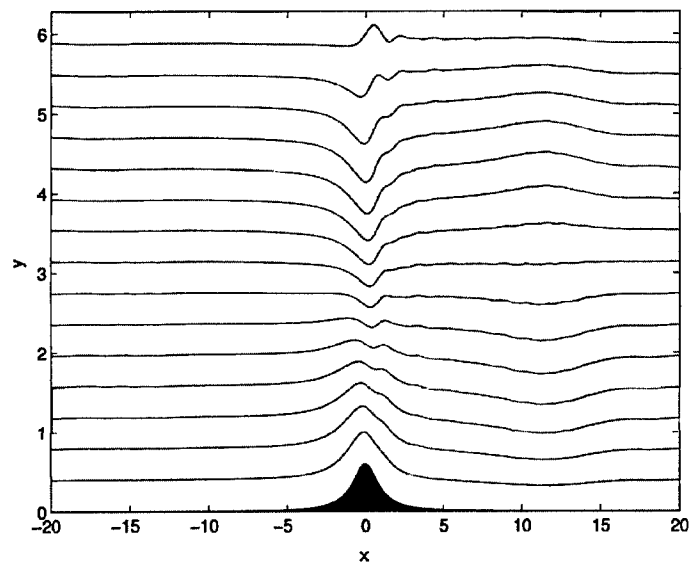


Fig. 8 Response at $t=150$ for the same flow parameters as in Fig. 7 but with $\phi=\pi/3$.

The results from numerical simulations of stratified flow over topography reported here suggest that periodic oscillations in the background buoyancy frequency cannot be ignored. A study of more general (quasi-periodic, unsteady) short-scale variations in the background flow conditions is currently under way.

Numerical method for unsteady computations

The unsteady Euler equations (2)–(4) were solved using the second-order projection method developed by Bell and co-workers [3–5]. Lamb [15] implemented this procedure to uniformly stratified finite-depth flow over locally confined topography and Skopovi [21] allowed for variations in the buoyancy-frequency profile. Here, we apply the numerical scheme to stratified flow of large depth over topography by introducing viscous layers that dissipate disturbances leaving the inviscid region and thus avoid reflections from the boundaries of the computational domain.

For this purpose, we solve the governing equations (2)–(4) with the viscous term $\nu(\mu^2 \mathbf{u}_{xx} + \mathbf{u}_{yy})$ added to the right-hand side of the momentum equation (4). Here ν denotes a spatially varying dimensionless viscosity that is distributed within viscous layers around the inviscid region. Specifically, near the upper boundary,

$$\nu = 0.1\mu^{-1} \sin\left(\frac{y - y_0}{60 - y_0} \frac{\pi}{2}\right), \quad (23)$$

so ν increases gradually from zero at the lower edge ($y = y_0$) to $\nu = 0.1\mu^{-1}$ at the upper edge ($y = 60$) of the viscous layer. The upper edge coincides with the top boundary of the computational domain. In the side layers, to ensure numerical stability at the inflow and outflow boundaries, the viscosity is first increased in a way analogous to (55), then is held constant at $0.1\mu^{-1}$ for M number of grid points and finally is brought back to zero again sinusoidally over the span of M points (see Skopovi [22] for details).

In all simulations, we used $y_0 = 41$, while $M = 50$ for computations with $\mu = 1/6$ and $M = 25$ for runs with $\mu = 0.05$. A typical contour plot of the viscosity profile is presented in Fig. 11 from which it is evident that nearly two thirds of the computational domain are occupied by absorbing layers. In order to accommodate the bottom boundary of the computational domain where we enforce the inviscid boundary condition (i.e. zero velocity perpendicular to the topography), viscosity in the lateral absorbing layers is linearly increased in the vertical direction from zero at the topography to the layer value over 20 grid points, as indicated by curving contours in the bottom left and right corners of Fig. 11.

The numerical method of solution was tested in various ways. First we verified that the nearly hydrostatic unsteady response for uniformly stratified flow over topography converges towards Long's steady-state solution. This was a rigorous test of the performance of the upper viscous layer, as in the absence of oscillations in the stratification profile, disturbances are not trapped so all energy is radiated upwards. Secondly, as a test of the lateral absorbing layers, we compared the response using viscous layers at $x = \pm 18$ against that obtained when the layers are positioned at $x = \pm 10$. Typical results are shown in Fig. 10 from which it is apparent that the layers are effectively absorbing waves exiting the inviscid region without impacting the flow field within the region of interest. We remark that this comparison is made at $t = 150$, which corresponds to the largest time at which we present our unsteady results. Lastly, we verified that our numerical results did not vary appreciably when the spatial resolution was changed.

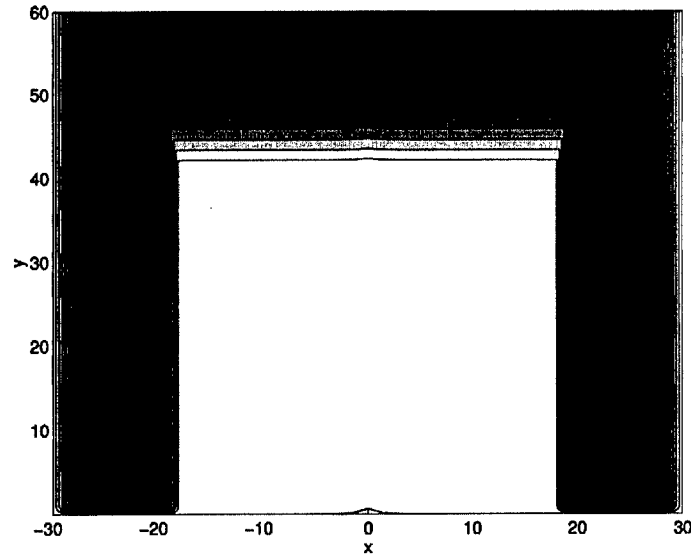


Fig. 9 Contour plot of the viscosity profile for simulations in Fig. 2. Viscosity is gradually increased from the inviscid region (white) to the maximum value $0.1\mu^{-1}$ (black).

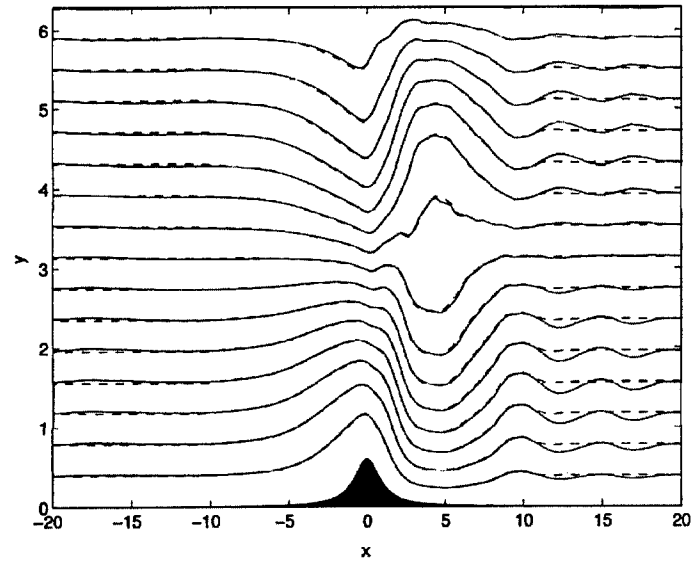


Fig. 10 Comparison of the resonant response for $F = 1$, $\mu = 1/6$, $\phi = 0$ and $t = 150$ when absorbing layers are positioned at $x = \pm 10$ (dashed line) with the response obtained for the same set of parameters when the inviscid region extends to $x = \pm 18$ (solid line).

Following Lamb [15], we have used a quadrilateral grid with the higher resolution in the vicinity of the obstacle. The grid is linearly stretched along both the horizontal and the vertical such that the height of the bottom cells is 15 times smaller than the height of the cells at the

upper boundary, while the width of the middle cells is 15 times smaller than the width of the left- and right-boundary cells for simulations where $\mu = 1/6$, and 10 times smaller for runs where $\mu = 0.05$. All simulations are carried out on a numerical domain that contains 245 cells in the vertical direction. In the horizontal direction, 1200 cells were used for flows with $\mu = 1/6$ and 800 cells for flows with $\mu = 0.05$. In all runs, the width of the numerical domain is $x \in [-30, 30]$ when $\mu = 1/6$ and $x \in [-15, 15]$ when $\mu = 0.05$. The only exception is the simulation in Fig. 10 with the viscous layers starting at $x = \pm 10$, which is produced with 860 cells in the horizontal direction and the lateral boundaries of the computational domain at $x = \pm 20$. Lastly, in regard to temporal discretization, upon impulsively accelerating the flow from rest, we use the time step $\Delta t = 0.015$ for runs with $\mu = 1/6$ and $\Delta t = 0.02$ with $\mu = 0.05$.

B. Effects of Temporal Variations in Wind Velocity on the Generation of Mountain Gravity Waves

The vast majority of previously conducted studies on the subject of stratified flows over topography, primarily for mathematical tractability and computational cost, assumes a constant background velocity. It is generally known, however, that a typical atmospheric free stream, in addition to exhibiting spatial variations, regularly fluctuates with time. In this study, we are interested in the effect of these temporal modulations.

On the theoretical side, one of the first comprehensive efforts to account for time variations in the wind velocity is the work of Bell [6] who in 1975 derived the linear steady-in-the-mean solution for a horizontally incident and sinusoidally oscillating background velocity with zero mean. He established that the equation governing his model is nonlinear with respect to the basic flow. As a result, internal gravity waves in his model were produced not only at the fundamental frequency, but also at all of its harmonics. Later, Bannon and Zehnder [2] constructed a model that is more appropriate for atmospheric conditions by adding a steady component to the sinusoidally varying free stream of Bell [6]. In spite of the fact that it is restricted to a hydrostatic mountain, their linear steady-in-the-mean solution encompassed the Coriolis acceleration and provided perhaps the first insight into the importance of temporal modulations in the atmospheric context by indicating that the instantaneous mountain drag may be larger than that exerted by the steady wind. We also cite the work of Hines [14] who allowed the steady portion of the background velocity to vary with height, but slowly so that the WKB approximation can be used to analyze the resulting flow field. Although Hines's linear analysis is the first substantial effort to consider simultaneously shear and unsteadiness in the basic flow, it is rather limited to a monochromatic mountain profile.

Among computational studies, we point out the work of Lott and Teitelbaum [18] who investigated the formation of unsteady linear gravity waves in a free stream that starts from zero and returns to zero after a finite time. Their analysis is limited to a monochromatic topography, but it includes effects of shear. We also acknowledge the work of Eckermann and co-workers [7] who, for the purpose of forecasting mountain waves in the field, recently devised a hybrid methodology. This approach combines linear theory to estimate the near-field response close to the topography with a ray-tracing technique that accounts for gradual variations of the buoyancy frequency and wind speed in the far field.

These previously conducted studies that account for temporal changes in the background velocity possess several limitations. Primarily, they are linear in nature and they neglect short-scale buoyancy frequency variations. In the work of Prasad and Akylas [20] and later Skopovi and Akylas [23], these mechanisms have been found to play a substantial role in shaping the character of the response with the steady free stream. At this point, therefore, a natural question to ask is how does the flow behave in the absence of these constraints. In an attempt to answer this question, we first derive the linear hydrostatic steady-in-the-mean solution for sinusoidally oscillating background velocity, which is valid for an arbitrary Brunt-Väisälä frequency. The solution and details of its numerical implementation are discussed in the following section. Furthermore, we construct a nonlinear computational model capable of sim-

ulating the flow field generated by the time-varying background flow. Implementation details of the model are presented. Equipped with these two tools, we explore the significance of nonlinearity by examining the response due to a gradually increasing background flow from zero to a constant value in the presence of uniform stratification. Following this effort, we turn our attention to 1–2 km modulations in the buoyancy frequency. We explore their importance by considering the transient response to the basic velocity that is the superposition of a uniform stream and harmonic oscillations. Specifically, we concentrate on frequencies that are of the order of the atmospheric Brunt–Väisälä frequency and finally we analyze the behavior at periods that are of the order of hours.

Linear Theory for Monochromatic Variations

We shall use the same non-dimensional formulation as in Prasad and Akylas [20] for inviscid incompressible flow over localized topography with horizontal lengthscale L and peak amplitude H . Denoting the upstream flow speed by U_0 and by N_0 the characteristic value of the Brunt–Väisälä (buoyancy) frequency, the flow is governed by three independent parameters

$$\mu = \frac{U_0}{N_0 L}, \quad \varepsilon = \frac{HN_0}{U_0}, \quad \beta = \frac{N_0 U_0}{g}, \quad (24)$$

g being the gravitational acceleration. The Boussinesq parameter β is a measure of stratification; the long-wave parameter μ and the amplitude parameter ε control dispersive and nonlinear effects, respectively.

Employing L and U_0/N_0 as the characteristic lengthscales along the horizontal (x -) and vertical (z -) directions, respectively, and L/U_0 as the timescale, the governing equations (in the Boussinesq limit, $\beta \rightarrow 0$) become

$$\left(\frac{\partial}{\partial t} + U \frac{\partial}{\partial x} \right) (\psi_{zz} + \mu^2 \psi_{xx}) - r_x = \varepsilon J(\psi, \psi_{zz} + \mu^2 \psi_{xx}), \quad (25a)$$

$$\left(\frac{\partial}{\partial t} + U \frac{\partial}{\partial x} \right) r + N^2 \psi_x = \varepsilon J(\psi, r), \quad (25b)$$

where $J(a, b) = a_x b_z - a_z b_x$. In these expressions, ψ is the perturbation stream function, which physically denotes the deflection of a streamline from the hydrostatic value it possesses far upstream of the obstacle. It is physically defined as $(u, \mu w) = (U + \varepsilon \psi_z, -\varepsilon \psi_x)$ where u and w are respectively horizontal and vertical velocity components. Moreover, $U(t)$ denotes the background flow velocity, N represents the buoyancy frequency while $\varepsilon \beta r$ is the pretrubation density.

In order to complete the mathematical formulation of the problem under consideration, we need to specify boundary conditions. Due to the fact that the topography is presumed to be locally confined in the horizontal direction and the fluid is considered to be infinitely deep, we require

$$\psi = 0 \text{ and } r = 0 \quad \text{at} \quad x = \pm\infty \text{ and } z = +\infty. \quad (26)$$

Along the bottom boundary, on the other hand, the velocity component perpendicular to the barrier is zero, which in turn implies that the scalar product of the velocity and the unit vector orthogonal to the mountain is zero. Algebraically, this can be written in terms of ψ as

$$-\psi_x = \frac{dh}{dx}(U + \varepsilon\psi_z) \quad \text{at} \quad z = \varepsilon h(x), \quad (27)$$

where $h(x)$ designates the topography profile. At this point, it is important to emphasize that in all simulations in this study, we use the topography profile

$$h = \frac{1}{1+x^2} \quad (28)$$

popularly known as the algebraic mountain or Witch of Agnesi.

We commence the derivation of the linear steady-in-the-mean solution that accommodates any stratification by defining the Fourier transform and its inverse with respect to x as

$$\mathfrak{F}\{\psi\} = \int_{-\infty}^{+\infty} \psi e^{-ikx} dx \quad \text{and} \quad \mathfrak{F}^{-1}\{\tilde{\psi}\} = \frac{1}{2\pi} \int_{-\infty}^{+\infty} \tilde{\psi} e^{ikx} dk. \quad (29)$$

Taking the transform (29) of our governing equations (25) in the limit $\varepsilon \rightarrow 0$ then yields

$$\left(\frac{\partial}{\partial t} + ikU\right)^2 (-k^2 \mu^2 \tilde{\psi} + \tilde{\psi}_{zz}) - N^2 k^2 \tilde{\psi} = 0. \quad (30)$$

Following Bell [6], (30) can be mathematically simplified by introducing the horizontal co-ordinate (ξ) traveling with the time-varying free stream. In terms of x and U , ξ is defined as

$$\xi = x - \int_0^t U(\tau) d\tau. \quad (31)$$

The relationship between $\tilde{\psi}$ and the Fourier transform with respect to ξ , denoted as $\hat{\psi}$, is then

$$\hat{\psi} = \tilde{\psi} e^{ik \int_0^t U(\tau) d\tau}. \quad (32)$$

Substituting (32) into (30) gives the linearized governing equation (25) in terms of $\hat{\psi}$ as

$$\hat{\psi}_{zzt} - k^2 \mu^2 \hat{\psi}_{tt} - N^2 k^2 \hat{\psi} = 0. \quad (33)$$

We construct the bottom boundary condition by inserting Fourier transform of (27) into (32) to obtain

$$\hat{\psi} = -\frac{\tilde{h}}{ik} \frac{\partial}{\partial t} \left(e^{ik \int_0^t U(\tau) d\tau} \right) \quad \text{at} \quad z = 0. \quad (34)$$

Here, \tilde{h} designates the Fourier transform of the ridge. Following Bannon and Zehnder [2], at this point, we restrict our considerations to the background velocity of the form

$$U = 1 + \Delta \cos(\omega_0 t) \quad (35)$$

where both Δ and ω_0 are constants. With this basic flow, the time derivative in (34) may be eliminated by introducing the Bessel functions of the first kind (J_n) defined by

$$\exp\left[\frac{y}{2}\left(q - \frac{1}{q}\right)\right] = \sum_{n=-\infty}^{+\infty} q^n J_n(y) \quad (36)$$

where n is an integer. For $\ln(q) = i\phi$, it follows that

$$e^{i y \sin \phi} = \sum_{n=-\infty}^{+\infty} e^{i \phi n} J_n(y). \quad (37)$$

Substitution of (35) and (37) into (34) with $y = k\Delta/\omega_0$ and $\phi = \omega_0 t$ leads to the bottom boundary condition

$$\hat{\psi} = -\tilde{h} \sum_{n=-\infty}^{+\infty} \frac{k + \omega_0 n}{k} J_n\left(\frac{k\Delta}{\omega_0}\right) e^{i(k + \omega_0 n)t} \quad \text{at } z = 0. \quad (38)$$

Based on (38), we seek the solution of (33) in the form

$$\hat{\psi} = \tilde{h} \sum_{n=-\infty}^{+\infty} W J_n\left(\frac{k\Delta}{\omega_0}\right) e^{i(k + \omega_0 n)t} \quad (39)$$

where W is the function dependent on z , k and n . Substitution of (39) into (33), reveals that W must satisfy the second order ordinary differential equation with respect to z

$$W_{zz} + k^2 \left[\frac{N^2}{(k + \omega_0 n)^2} - \mu^2 \right] W = 0. \quad (40)$$

Before discussing a varying stratification, we consider the case of constant Brunt–Väisälä frequency. In this scenario, the solution of (40) can be determined analytically and it takes the form

$$W = \mathbb{C}_1 e^{imz} + \mathbb{C}_2 e^{-imz} \quad (41)$$

with m given by

$$m = \left[\frac{k^2 N^2}{(k + \omega_0 n)^2} - k^2 \mu^2 \right]^{\frac{1}{2}}. \quad (42)$$

In (41), \mathbb{C}_1 and \mathbb{C}_2 are functions of k and n . They are determined from (38) and the top boundary condition.

The form of the upper boundary condition for each k and n depends on whether (41) is exponential or oscillatory in nature. It is exponential if $N^2/(k + \omega_0 n)^2 - \mu^2 < 0$. In this case, the portion of (41) that grows with height is physically unrealistic and it is neglected by setting $\mathbb{C}_2 = 0$. The solution of (41) then becomes

$$W = \mathbb{C} e^{imz} \quad \text{with} \quad m = i \left| \frac{k}{k + \omega_0 n} \right| \sqrt{\mu^2 (k + \omega_0 n)^2 - N^2} \quad (43)$$

with $\mathbb{C} = \mathbb{C}_1$. If $N^2/(k + \omega_0 n)^2 - \mu^2 > 0$, (41) is oscillatory. In this regime, (39) indicates that $\hat{\psi}$ is the superposition of plane waves with the frequency $\omega = -(k + \omega_0 n)$ and the vertical wavenumber that is either a positive or negative quantity (42). The proper sign of m for each k and n is determined from the radiation condition, which states that $\partial\omega/\partial m > 0$. In terms of ω_0 , k and n , this can be expressed as

$$\frac{\partial\omega}{\partial m} = \frac{m(k + \omega_0 n)}{m^2 + \mu^2 k^2} > 0. \quad (44)$$

Due to the fact that the denominator of this inequality is always greater than zero, the group velocity is positive and all energy is radiated outwards if the sign of m coincides with that of $k + \omega_0 n$. Consequently, in the oscillatory regime, (41) may be written as

$$W = \mathbb{C}e^{imz} \quad \text{with} \quad m = \frac{|k|}{k + \omega_0 n} \sqrt{N^2 - \mu^2(k + \omega_0 n)^2} \quad (45)$$

where \mathbb{C} is either \mathbb{C}_1 or \mathbb{C}_2 depending on the sign of $k + \omega_0 n$. In (43) and (45), \mathbb{C} is determined from (38) to be

$$\mathbb{C} = -\frac{k + \omega_0 n}{k}. \quad (46)$$

The linear steady-in-the-mean solution for constant N and U given by (35) may now be written as

$$\psi = \frac{1}{2\pi} \int_{-\infty}^{+\infty} \tilde{h} \sum_{n=-\infty}^{+\infty} W J_n \left(\frac{k\Delta}{\omega_0} \right) e^{i[kx + mz - k\Delta/\omega_0 \sin(\omega_0 t) + \omega_0 n t]} dk \quad (47)$$

where W is determined from (43) and (45).

It can be easily verified that for the uniform basic velocity ($\Delta = 0$) and $N = 1$, the hydrostatic limit ($\mu \rightarrow 0$) of (47) reduces to the linear solution of Long [17]. Moreover, in the absence of the time-invariant component of the free stream (35), (47) is equivalent to the equation governing the model of Bell [6]. Lastly, (47) is analogous to the solution of Bannon and Zehnder [2] when the Coriolis acceleration in their model is neglected.

The solution (47) can be computed by using Gaussian quadrature to evaluate the integral for each n . In that regard, it is important to note that $k = 0$ is an integrable singularity. In fact, using l'Hôpital's rule, one can demonstrate that the limit $k \rightarrow 0$ of the integrand is finite for all n regardless of stratification.

The solution of (40) for a varying buoyancy frequency must be determined numerically. While the bottom boundary condition is given by (38) regardless of the stratification, the upper boundary condition for constant N can still be used if, following Davis [8], we assume that above some height $z = z_\infty$, $N = N_\infty$. For numerical simplicity, we additionally restrict our considerations to the hydrostatic response ($\mu \rightarrow 0$). With these two assumptions, the upper boundary condition for constant N is given by

$$W = \mathbb{C}e^{i\frac{|k|N_\infty}{k + \omega_0 n} z_\infty}, \quad (48)$$

and its z -derivative is

$$W_z = \mathbb{C} \frac{i|k|N_\infty}{k + \omega_0 n} e^{i \frac{|k|N_\infty}{k + \omega_0 n} z_\infty}. \quad (49)$$

We solve (40) by first guessing the value of \mathbb{C} in (48) and (49). From the knowledge of W and W_z at $z = z_\infty$, we then use the fourth order Runge–Kutta method to attain W at $z = 0$. The difference between this computed value, denoted here as W_0 , and that required by the bottom boundary condition (38) gives the error associated with our guess, namely,

$$E_{err}(\mathbb{C}) = W_0(\mathbb{C}) + \frac{k + \omega_0 n}{k}. \quad (50)$$

We update this guess via Newton–Raphson scheme. In particular, the new guess is given by

$$\mathbb{C}^{new} = \mathbb{C} - \frac{E_{err}(\mathbb{C})}{E'_{err}(\mathbb{C})}. \quad (51)$$

Here, E'_{err} is the approximation of the error function's derivative at \mathbb{C} obtained from

$$E'_{err}(\mathbb{C}) = \frac{E_{err}(\mathbb{C} + \delta) - E_{err}(\mathbb{C})}{\delta} \quad (52)$$

where δ is a small perturbation to \mathbb{C} . Once we obtain W for each k and n , we evaluate (47) using Gaussian quadrature analogous to the case of constant N .

In all simulations presented in this document, we use $k \in [-15, 15]$ with the grid spacing of 0.025. Moreover, we choose the range of n in such a way that for all values of n outside this range $J_n(k\Delta/\omega_0) < 10^{-5}$. In all computations involving a varying stratification, we use $\delta = 10^{-5}$ and the initial guess $\mathbb{C} = -(k + \omega_0 n)/k$. We iterate the Newton–Raphson scheme until $|E_{err}| < 10^{-3}$.

The numerical method for non-uniform N was tested in two ways. First, we verified that for $N = 1$ and $\Delta = 0$, the solution coincides with that of Long [17]. Moreover, for $\Delta = 0$ and a two-layer buoyancy frequency, we confirmed the agreement with the linear ($\epsilon \rightarrow 0$) limit of the response of Durran [9].

Numerical method for unsteady computations

In this study, we solve the unsteady Euler equations (25) using the second-order projection method developed by Bell and co-workers [3–5]. Lamb [16] implemented this procedure to uniformly stratified finite-depth flow over locally confined topography and Skopovi [21] allowed for variations in the buoyancy-frequency profile. In the further development, Skopovi and Akylas [23] applied the numerical scheme to stratified flow of large depth over topography by introducing viscous layers that dissipate disturbances leaving the inviscid region and thus avoid reflections from the boundaries of the computational domain. Here, we additionally extend the scheme to encompass temporal variations in the background velocity.

We implement the time modulations of the free stream velocity U by adding the forcing function $b(t)$ to the right-hand side of the horizontal component of the momentum equation.

This term physically denotes the local time rate of change of the spatially uniform horizontal background velocity. Therefore, accommodating a particular temporal variation in the basic flow, from the numerical standpoint, merely entails specifying this forcing function. In this study, we are concerned with a free stream, U , that is the sum of a homogeneous profile and a monochromatic time-varying component of amplitude Δ and frequency ω_0 . We computationally achieve this variation via the forcing function

$$b = \begin{cases} \frac{\pi(1+\Delta)}{2t_a} \sin\left(\frac{\pi}{t_a}t\right) & \text{if } t \leq t_a, \\ -\Delta \omega_0 \sin[\omega_0(t-t_a)] & \text{if } t > t_a. \end{cases} \quad (53)$$

We accelerate the flow from rest so that $U(0)=0$ and therefore (53) yields

$$U = \begin{cases} \frac{1+\Delta}{2} \left[1 - \cos\left(\frac{\pi}{t_a}t\right) \right] & \text{if } t \leq t_a, \\ 1 + \Delta \cos[\omega_0(t-t_a)] & \text{if } t > t_a. \end{cases} \quad (54)$$

The first portion of (53) increases U sinusoidally from zero to some finite value, which in this study is $1+\Delta$; thereupon, U is varied harmonically. The gradual turning on of the flow for $t \leq t_a$, is necessary to ensure the continuity of the forcing function and therefore provide the numerical stability of our scheme.

Following Skopovi and Akylas [23], we implement open boundary conditions (26) by solving the governing equations (25) with the viscous terms added to the right-hand side of (25a). The kinematic viscosity (ν) is spatially varying within the viscous layers surrounding the inviscid region of interest. Specifically, near the upper boundary, we let

$$\nu = 0.1\mu^{-1} \sin\left(\frac{z-z_0}{Z-z_0} \frac{\pi}{2}\right), \quad (55)$$

so ν increases gradually from zero at the lower edge ($z=z_0$) to $\nu=0.1\mu^{-1}$ at the upper edge ($z=Z$) of the viscous layer. The upper edge coincides with the top boundary of the computational domain. In the side layers, to ensure numerical stability at the inflow and outflow boundaries, the viscosity is first increased in a way analogous to (55), then is held constant at $0.1\mu^{-1}$ for 50 grid points and finally is brought back to zero again sinusoidally over the span of 50 points (see Skopovi [22] for details). In all simulations, we used $z_0=41$. A typical contour plot of the viscosity profile is presented in Fig. 11 from which it is evident that nearly two thirds of the computational domain are occupied by absorbing layers. In order to accommodate the bottom boundary of the computational domain where we enforce the inviscid boundary condition (i.e. zero velocity perpendicular to the topography), viscosity in the lateral absorbing layers is linearly increased in the vertical direction from zero at the topography to the layer value over 20 grid points, as indicated by curving contours in the bottom left and right corners of Fig. 11.

Following Lamb [16], we have used a quadrilateral grid with the higher resolution in the vicinity of the obstacle. The grid is linearly stretched along both the horizontal and the vertical

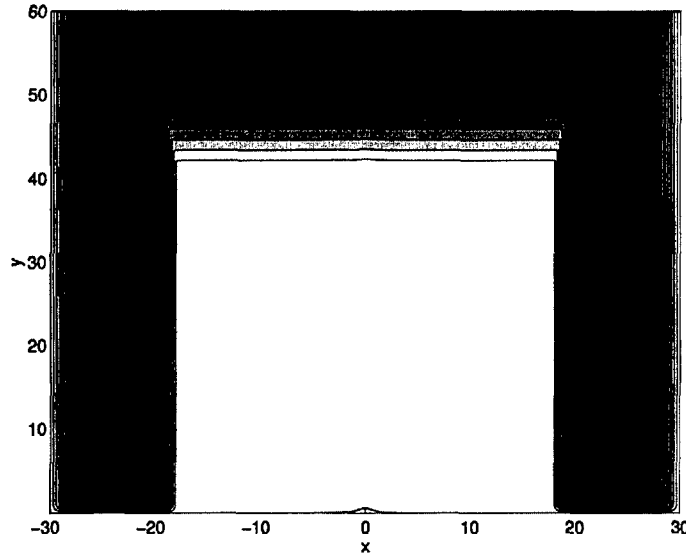


Fig. 11 A typical contour plot of the viscosity profile. Viscosity is gradually increased from the inviscid region (white) to the maximum value $0.1\mu^{-1}$ (black).

such that the height of the bottom cells is 15 times smaller than the height of the cells at the upper boundary, while the width of the middle cells is 15 times smaller than the width of the left- and right-boundary cells. All simulations are carried out on a numerical domain that contains 245 cells in the vertical direction for flows with $Z=60$ and 205 cells for flows with $Z=50$. In the horizontal direction, 1200 cells were used for flows with $Z=60$ and 860 cells for flows with $Z=50$ while the width of the numerical domain is $x \in [-30, 30]$ when $Z=60$ and $x \in [-22, 22]$ when $Z=50$. Lastly, in regard to temporal discretization, upon impulsively accelerating the flow from rest, we use the time step $\Delta t = 0.015$.

The computational approach was tested in three ways. We first examined the performance of viscous layers by comparing the behavior for the inviscid domain bounded by $x = \pm 10$ and $z = 50$ to that obtained with boundaries positioned at $x = \pm 20$ and $z = 60$. A comparison between responses with $\varepsilon = 0.6$, $\mu = 1/6$, $t_a = 0.05\mu$ and $\omega_0 = 12$ is presented in Fig. 12. Results suggest that even with $\Delta = 0.75$, layers at $x = \pm 10$ are effectively dissipating disturbances by negligibly influencing streamline patterns within the inviscid region. This comparison is conducted at $t = 100$, which is the largest time associated with our simulations involving the varying free stream.

As the second test, we confirmed that the computation in Fig. 12 reaches the steady state and holds it for a substantial amount of time. The comparison between responses at $t = 83$ and $t = 100$ is shown in Fig. 13. It is evident from the figure that steady conditions are reached by $t = 83$ and that the model is holding this state extremely well.

As the last check, we verified that in the limit $\varepsilon \rightarrow 0$ the flow field with $\Delta = 0.75$ and $\omega_0 = 12$ approaches the steady-in-the-mean solution predicted by the theory derived in the previous

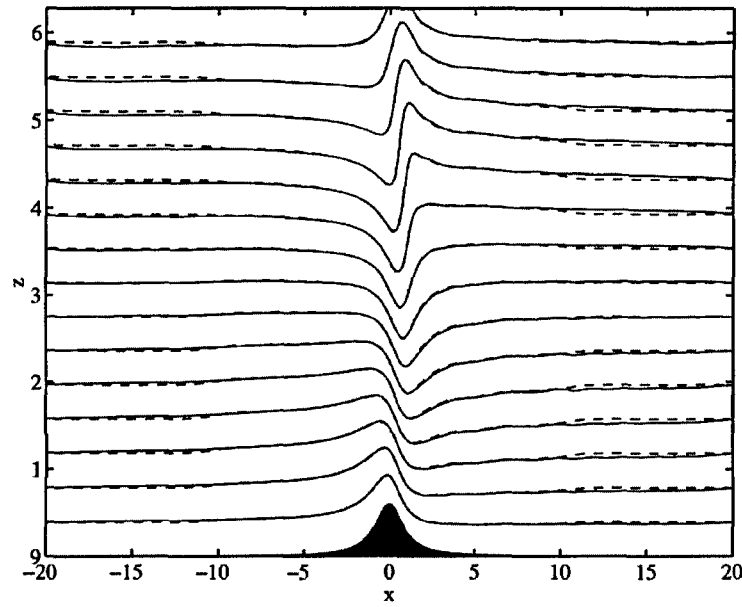


Fig. 12 Comparison of the response for $\varepsilon = 0.6$, $\mu = 1/6$, $\Delta = 0.75$, $\omega_0 = 12$, $t_a = 0.05\mu$ and $t = 100$ when absorbing layers are positioned at $x = \pm 10$ (dashed lines) with that obtained for the same set of parameters when the inviscid region extends to $x = \pm 18$ (solid lines).

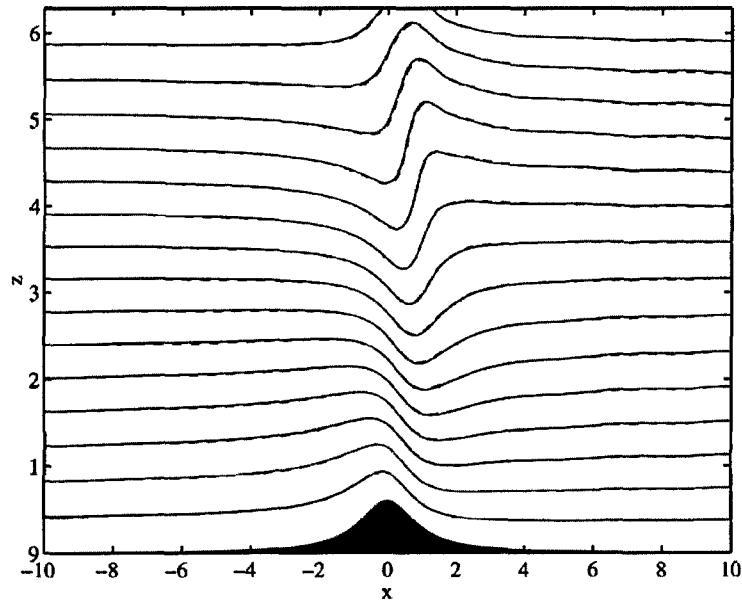


Fig. 13 Evolution of the flow field for $\varepsilon = 0.6$, $\mu = 1/6$, $\Delta = 0.75$, $t_a = 0.05\mu$ and $\omega_0 = 12$: dashed lines $t = 83$, solid lines $t = 100$.

section. The agreement for $\varepsilon = 0.2$, $\mu = 1/6$, and $t_a = 0.05\mu$ is presented in Fig. 14(a). With an increase in ε to 0.6, nonlinearity becomes important and the two responses grow apart as illustrated in 14(b).

We end the discussion of unsteady numerics by reporting that our formulation of the dissipative layer technique did not work in the absence of the uniform stream, that is, when $U = \cos(\omega_0 t)$. Under these circumstances, our computations were blowing up. We did not explore the reasons behind this malfunction because, as pointed out by Lott and Teitelbaum [18], the case of reversing background flow is not extremely relevant to atmospheric conditions that we are concerned with in this study.

Gradually Accelerated Background Velocity

We explore the significance of nonlinearity in flows featuring temporal variations in the free stream by gradually increasing the basic velocity according to (54) with $\Delta = 0$. Here, t_a then physically denotes the time required to accelerate U from rest to its terminal value $U = 1$. Due to the fact that following the initial acceleration the background flow is kept constant, we expect the response to approach the steady-state solution for $U = 1$, which is that of Long [17]. With μ fixed, the problem under consideration is governed by two parameters, namely, ε and t_a . As it is customary for a two-variable problem, we conduct the analysis by first holding t_a constant and varying ε . Subsequently, we fix ε and allow for changes in t_a . In each case, we contrast the resulting response to that obtained with the same value of ε and $t_a = 0.05\mu$, which simulates the impulsive startup.

Our fully nonlinear simulations indicate that in the limit of the vanishing topography height ($\varepsilon \rightarrow 0$), there is a negligible difference between the impulsive and the slowly accelerated behavior. This is evident from the comparison of responses for $\varepsilon = 0.2$ and $\mu = 1/6$ presented in Fig. 15. The contrast at $t = 40$ in Fig. 15(a), an instant when the gradually increased free-stream velocity has just reached its terminal value, reveals negligible difference in streamline amplitudes and steepness directly above the barrier. The patterns differ, however, in the lee of the obstacle and this discrepancy is due to transients of the slowly accelerated response, which at this time are still present in the domain of interest. They depart by $t = 60$ (Fig. 15(b)) and after this point the two flow fields coincide.

An increase in ε to 0.6 while keeping μ and t_a constant, generates a profound difference between the two responses. Particularly, at $t = 40$, as depicted in Fig. 16(a), streamline amplitudes of the slowly initiated flow are now nearly twice as large as their rapidly actuated analogues. Although in this simulation wave breaking did not occur, we note that streamlines corresponding to the accelerated field are much steeper and are nearly at the point of overturning. As transients move out, the progressively excited behavior once again approaches its impulsive counterpart. In comparison to the previously discussed case with $\varepsilon = 0.2$, however, steady state is reached at a much later time, $t = 140$, as indicated in Fig. 16(b).

The described behavior for the fixed ε and two different acceleration times, 0.05μ and 40, suggests that for each value of t_a there is a distinct nonlinearity parameter for which wave breaking takes place. Correspondingly, we have further utilized our unsteady numer-

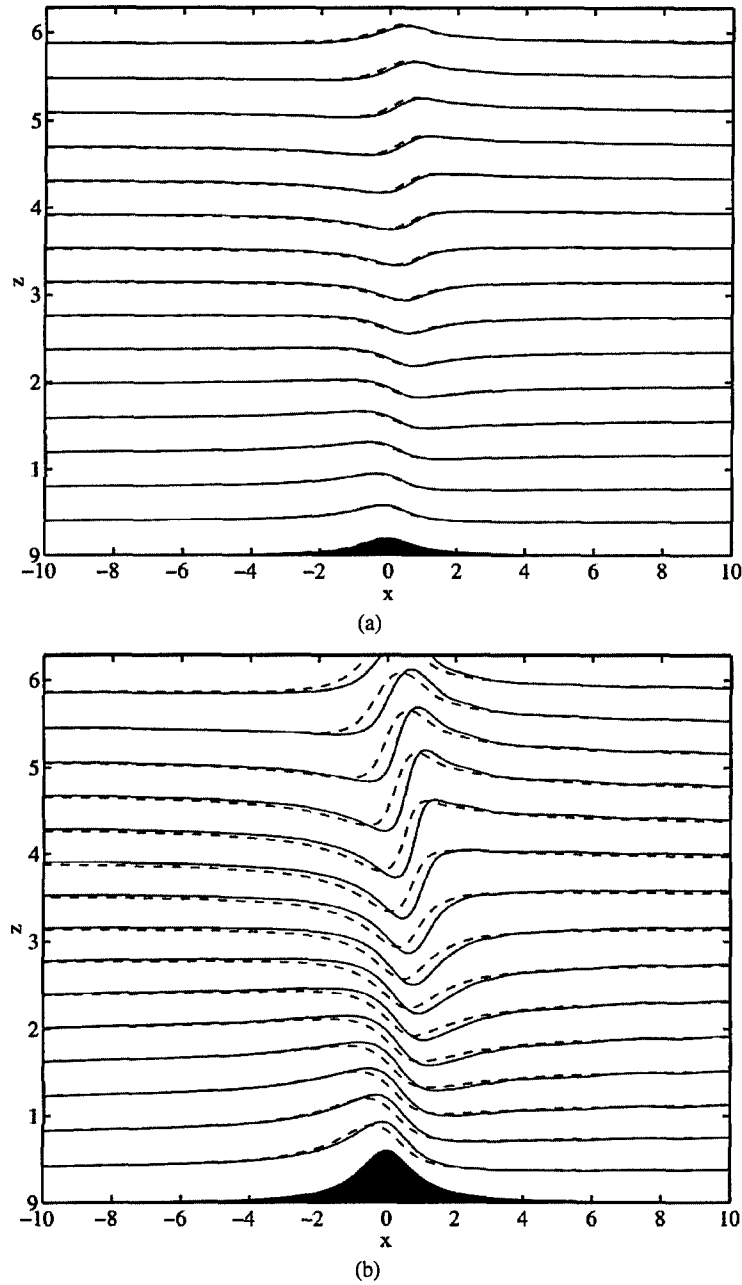


Fig. 14 Comparison of the behavior predicted by the unsteady model at $t = 100$ (solid lines) and that forecasted by the linear steady-in-the-mean theory (dashed lines) for $\mu = 1/6$, $\Delta = 0.75$, $\omega_0 = 12$ and $t_a = 0.05\mu$ (a) $\epsilon = 0.2$; (b) $\epsilon = 0.6$.

ical model to build the diagram in Fig. 17 that illustrates this relationship for $\mu = 1/6$. As anticipated, the chart indicates that as the value of ϵ decreases, it takes larger t_a to produce

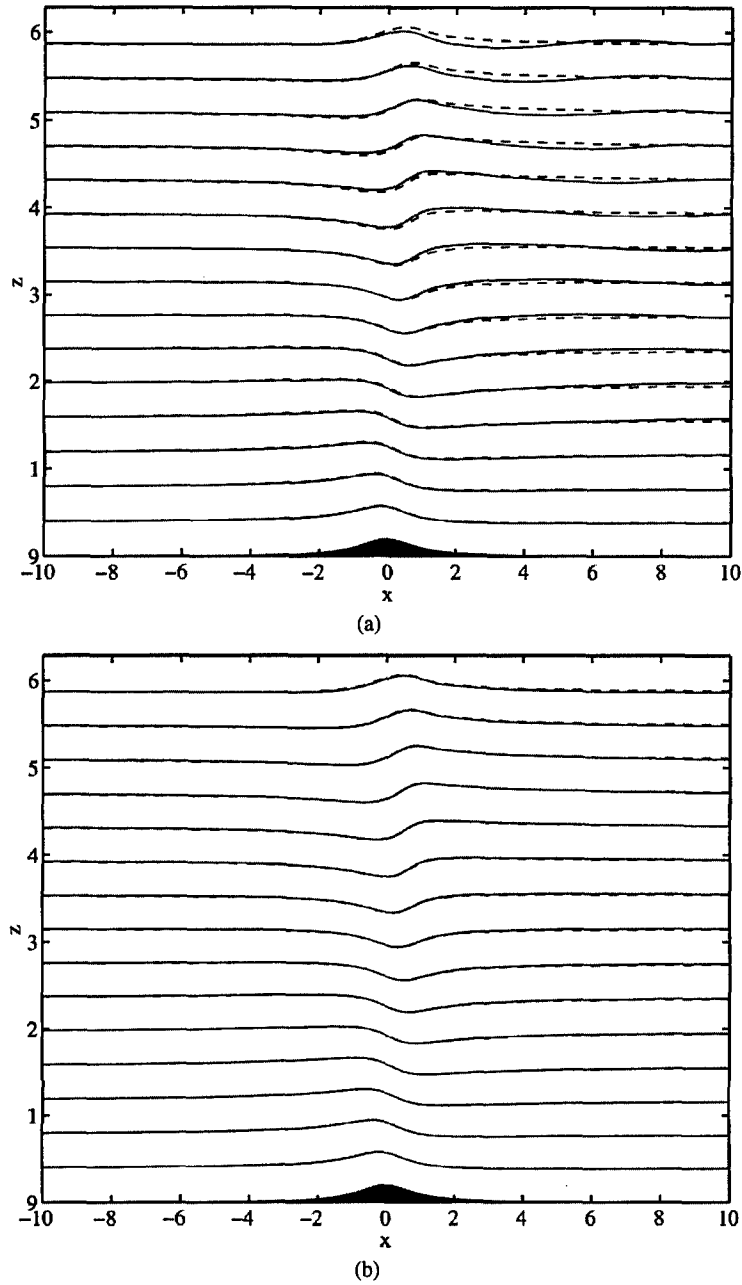


Fig. 15 Comparison of slowly (solid lines) and impulsively (dashed lines) accelerated streamline patterns for $\varepsilon=0.2$, $\mu=1/6$ and $t_a=40$ at (a) $t=40$; (b) $t=60$.

breaking. It is important to point out that we did not pursue computations for values of ε that are less than 0.6 as their corresponding acceleration times are physically meaningless.

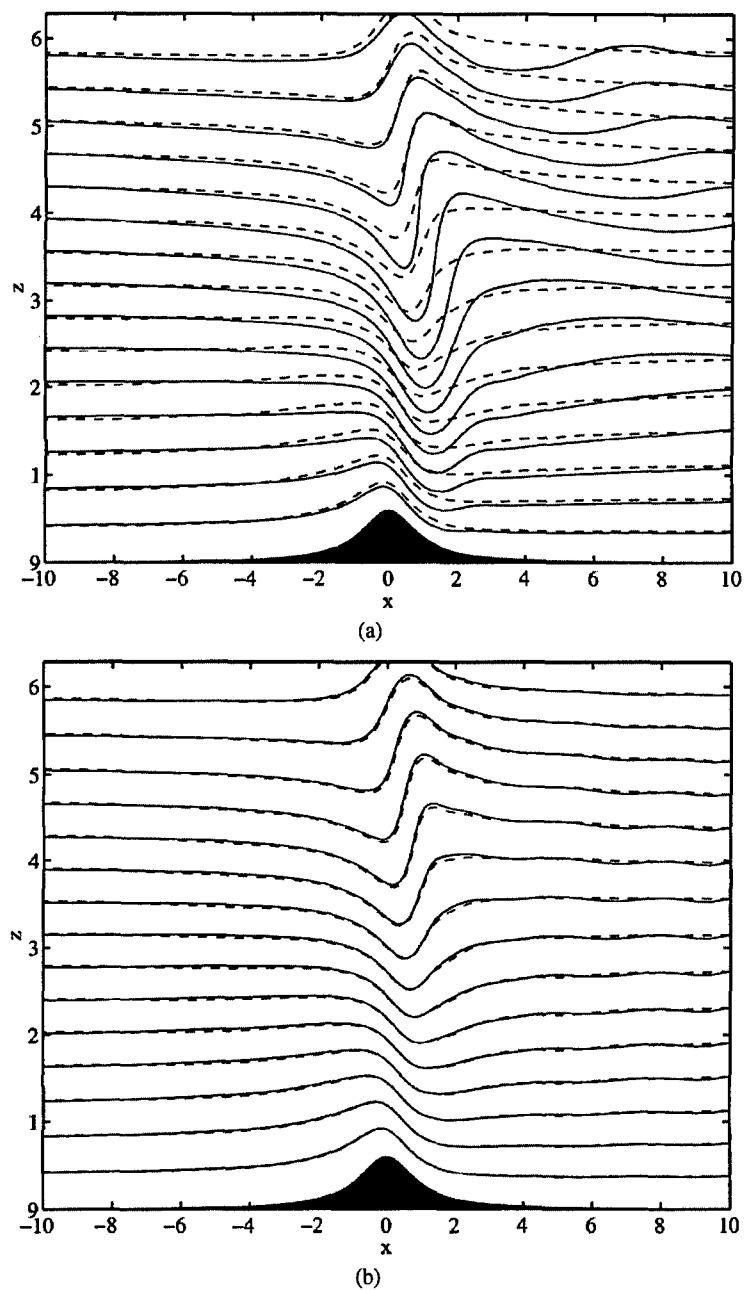


Fig. 16 Comparison of slowly (solid lines) and impulsively (dashed lines) accelerated streamline patterns for $\epsilon=0.6$, $\mu=1/6$ and $t_a=40$ at (a) $t=40$; (b) $t=140$.

This is because they are of the order of a day(s) and, as mentioned earlier, we expect these flows to typically last for several hours or less. We lastly stress that the attained acceleration

times are accurate within ± 2 of the plotted values. This tolerance is indicated by the error bars surrounding each point on the graph. They were obtained by refining the resolution of the simulation for $\varepsilon = 0.6$ until the breaking time did not significantly change any longer. The computed points are also dependent on the long-wave parameter although for $0 < \mu < 1/6$ this dependency is expected to be mild. This conclusion is based on the fact that the hydrostatic solution wave-breaks for $\varepsilon = 0.85$ while its counterpart with $\mu = 1/6$ breaks at the slightly lower value, $\varepsilon = 0.82$.

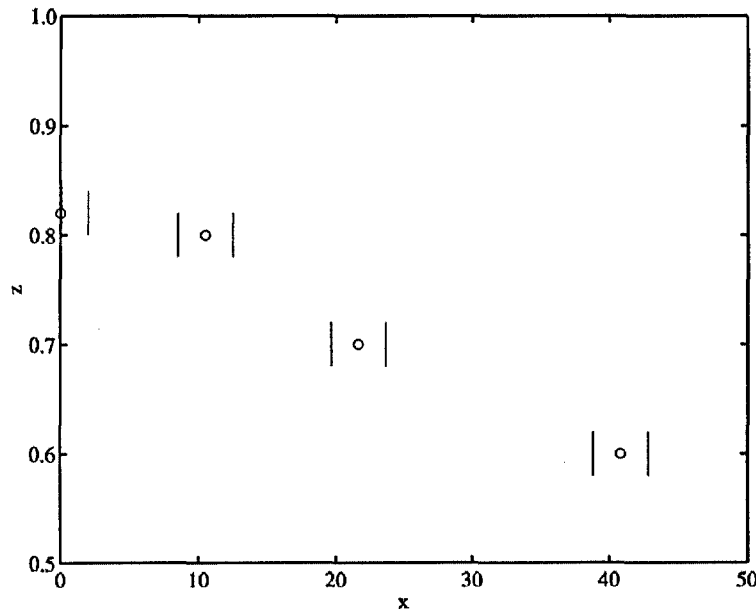


Fig. 17 Wave breaking as a function of the nonlinearity parameter and the time to acceleration for $\mu = 1/6$.

The underlying conclusion of this investigation is that temporal variations in the incident flow in combination with nonlinearity may give rise to large amplitude transients, which are ignored by the previously constructed models. As a result, these earlier efforts underestimate the size of the topography generated atmospheric buoyancy waves.

High-Frequency Sinusoidal Modulations

We now turn to an investigation of the flow field generated when the background velocity, in accordance with (35), is a superposition of a uniform stream and monochromatic temporal variations. In discussing these flows, we limit our considerations to oscillation amplitudes that are smaller than the steady component ($\Delta < 1$), so that the basic velocity does not experience a change in direction. Moreover, in this section, we concentrate on the high-frequency regime ($\omega_0 \rightarrow \infty$) of these modulations and we postpone the analysis of general frequencies to the next section.

In the limit $\omega_0 \rightarrow \infty$, the steady-in-the-mean solution (47) for a uniform stratification and $\mu \rightarrow 0$, as analytically demonstrated by Bannon and Zehnder [2], is identical to the behavior with the incident wind $U = 1$. In other words, the transience in the background velocity does not impact the response; hence, at time instances when the basic flow is unity, (47) coincides with the linear solution of Long [17]. Our numerical simulations reveal that with $\Delta = 0.75$, the two hydrostatic streamline patterns essentially coincide when ω_0 is roughly 200. As the value of μ increases, however, the frequency at which the agreement between the behavior with $\Delta = 0$ and that with $\Delta = 0.75$ takes place rapidly diminishes. In particular, according to our computations, for $\mu = 1/6$, the accord is reached when $\omega_0 = 6$, which upon the conversion to the dimensional form corresponds to the atmospheric Brunt-Väisälä frequency. We also find that aforementioned conclusions are unaffected by variations in the buoyancy frequency as the steady-in-the-mean solution (47) for $\Delta = 0.75$ and $\omega_0 = 6$ matches the linear ($\varepsilon \rightarrow 0$) response of Davis [8] when the stratification is given by

$$N = 1.5 + 0.5 \tanh[c(z - d)]. \quad (56)$$

with $c = 2$ and $d = 3$.

The behavior exhibited by the linear response also persists in the nonlinear regime. This is concretely evident from the comparison of the resonant flow field in Fig 2(a) of Skopovi and Akylas [23] with that obtained for the same stratification profile and the background velocity (54) when $t_a = 0.05\mu$, $\Delta = 0.75$ and $\omega_0 = 12$. The plot of the two flow fields at $t = 100$, illustrated in Fig. 18, reveals that streamline patterns are nearly identical.

We lastly point out that in agreement with conclusions of the previous section, we find that the amplitude of transients produced by temporal variations in the basic velocity increases with the decrease in ω_0 . This feature dominates at lower frequencies of temporal free-stream oscillations, which we consider next.

General Frequencies

In this section, we discuss the flow field produced when the modulation frequency in (35) is of the order of few hours. As before, we conduct the analysis by first examining properties of the linear steady-in-the-mean solution (47) and then we consider the effects of the nonlinearity and transients.

When the frequency of monochromatic modulations in (35) is $\omega_0 = 0.35$ and $\mu = 1/6$, the steady-in-the-mean solution (47) qualitatively retains the properties of the response with the uniform incident velocity. Particularly, in the presence of the resonant buoyancy frequency given by

$$N^2(z) = 1 + \mu^2 \{0.25 \sin(2z)\}. \quad (57)$$

the solution for $\Delta = 0.75$ exhibits the resonant behavior in a sense that the output of our numerical algorithm does not converge to a physically realistic solution. We were unable to verify if the resonance persists at lower values of ω_0 as these simulations necessitate a larger range of n , which in turn increases the cost of our simulations.

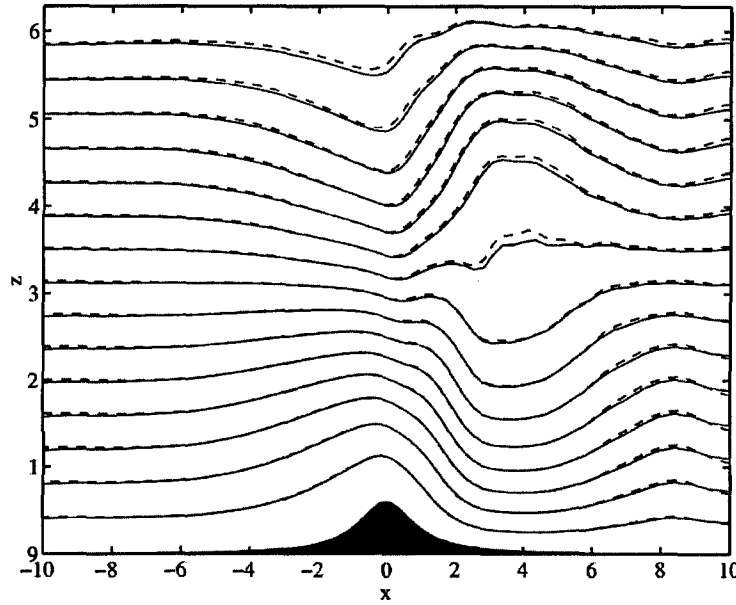


Fig. 18 Comparison between the response with the uniform (dashed lines) and monochromatically varying (solid lines) basic velocity for $\varepsilon=0.6$, $\mu=1/6$, $\Delta=0.75$, $\omega_0=12$, $t_a=0.05\mu$, $F=1$ and $\phi=0$ at $t=100$.

In addition, our computations indicate that the hydrostatic limit of (47) for $\omega_0=0.35$ and $\Delta=0.75$, analogous to models of Davis [8] and Durran [9], can be tuned by adjusting the tropopause height. For the stratification profile (56) with $c=2$ and $d=3$, we find that in the range $d \in [2, 2\pi]$ the response is maximized when $d=3\pi/2$ and minimized for $d=3\pi/4$ (Fig. 19). These values are in contrast to the $\omega_0 \rightarrow \infty$ limit where the linear flow field is tuned or detuned depending on whether d is an even or an odd multiple of $\pi/2$ respectively.

In accordance with our findings earlier, gradual monochromatic temporal free-stream modulations in the presence of nonlinearity produce transients whose amplitude grows with time. This is concretely demonstrated in Fig. 20, which compares the response for $\varepsilon=0.6$, $\mu=1/6$ and $t_a=0.05\mu$ at two different times, namely, 2.5 and 12.5, when the background flow in Fig. 20(a) modulates with the amplitude $\Delta=0.75$ and the frequency $\omega_0=0.63$. The two times are therefore exactly one period of the incident flow oscillations apart. It is evident from Fig. 20(b) that streamlines corresponding to $t=12.5$ are much larger in amplitude and steeper than those associated with $t=2.5$. This in turn suggests that similar to the resonant buoyancy frequency oscillations studied earlier, gradual variations in the basic velocity may produce overturning of density contours well below the critical amplitude of the topography predicted by the model of Long [17]. Unfortunately, we were unable to carry this simulation to the point of wave breaking as transients generated by the gradual basic flow variations eventually become so large that our viscous layers are unable to absorb them even with an increase in the value of ν .

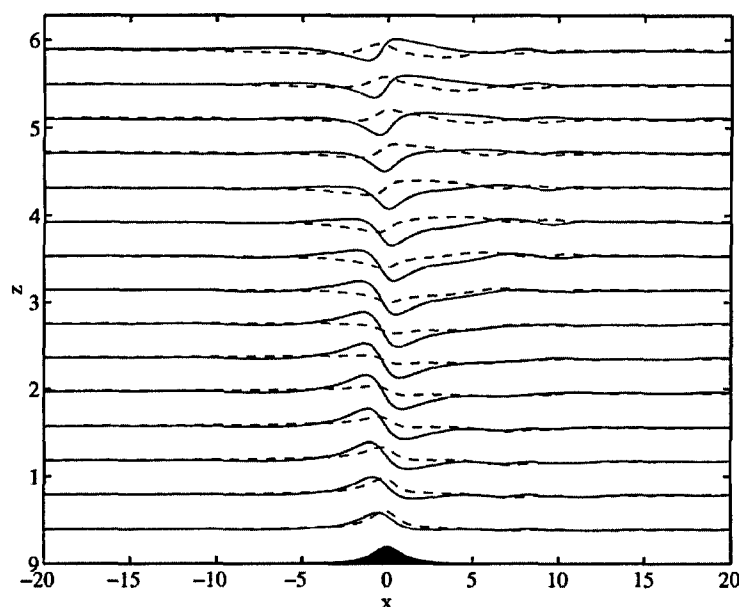


Fig. 19 Linear steady-in-the-mean solution for $\varepsilon=0.2$, $\mu=1/6$, $\Delta=0.75$ and $\omega_0=0.35$ when the buoyancy frequency is given by (56) with $c=2$: $d=3\pi/2$ (solid lines) and $d=3\pi/4$ (dashed lines).

References

1. Baines, P.G.: Topographic effects in stratified flows. Cambridge University Press, New York (1995)
2. Bannon, P.R., Zehnder, J.A.: Surface pressure and mountain drag for transient airflow over a mountain ridge. *J. Atmos. Sci.* **42**, 2454–2462 (1985)
3. Bell, J.B., Colella, P., Glaz, H.M.: A second-order projection method for the incompressible Navier-Stokes equations. *J. Comput. Phys.* **85**, 257–283 (1989)
4. Bell, J.B., Marcus, D.L.: A second-order projection method for variable-density flows. *J. Comput. Phys.* **101**, 334–348 (1992)
5. Bell, J.B., Solomon, J.M., Szymczak, W.G.: A second-order projection method for the incompressible Navier-Stokes equations on quadrilateral grids. AIAA 9th Computational Fluids Dynamics Conference. Buffalo, NY, June 14–16 (1989)
6. Bell, T.H.: Lee waves in stratified flows with simple harmonic time dependence. *J. Fluid Mech.* **67**, 705–722 (1975)
7. Broutman, D., Rottman, J.W., Eckermann, S.D.: A hybrid method for wave propagation from a linearized source, with application to mountain waves. *Q. J. R. Meteorol. Soc.* **127**, 129–146 (2001)
8. Davis, K.S.: Flow of nonuniformly stratified fluid of large depth over topography. Master's thesis, MIT (1999)
9. Durran, D.R.: Two-layer solutions to Long's equation for vertically propagating mountain waves: how good is linear theory? *Q. J. R. Meteorol. Soc.* **118**, 415–433 (1992)
10. Eckermann, S.D., Broutman, D., Tan, K.A., Preusse, P., Bacmeister, J.T.: Mountain waves in the stratosphere. NRL Review NRL/PU/7641-00-411 (2000)
11. Eckermann, S.D., Preusse, P.: Global measurements of stratospheric mountain waves from space. *Science* **286**, 1534–1537 (1999)
12. Grimshaw, R., Zengxin, Y.: Resonant generation of finite-amplitude waves by the flow of a uniformly stratified fluid over topography. *J. Fluid Mech.* **229**, 603–628 (1991)
13. Grimshaw, R.H.J., Smyth, N.: Resonant flow of a stratified fluid over topography. *J. Fluid. Mech.* **169**, 429–464 (1986)
14. Hines, C.O.: Modulated mountain waves. *J. Atmos. Sci.* **52**, 602–606 (1995)
15. Lamb, K.G.: Numerical simulations of stratified inviscid flow over a smooth obstacle. *J. Fluid Mech.* **260**, 1–22 (1994)
16. Lamb, K.G.: Numerical simulations of stratified inviscid flow over a smooth obstacle. *J. Fluid Mech.* **260**, 1–22 (1994)
17. Long, R.R.: Some aspects of the flow of stratified fluids. I. A theoretical investigation. *Tellus* **5**, 42–57 (1953)
18. Lott, F., Teitelbaum, H.: Topographic waves generated by a transient wind. *J. Atmos. Sci.* **50**, 2607–2624 (1993)
19. Phillips, O.M.: The interaction trapping of internal gravity waves. *J. Fluid Mech.* **34**, 407–416 (1968)
20. Prasad, D., Akylas, T.R.: Wave trapping and upstream influence in stratified flow of large depth. *J. Fluid Mech.* **491**, 301–324 (2003)

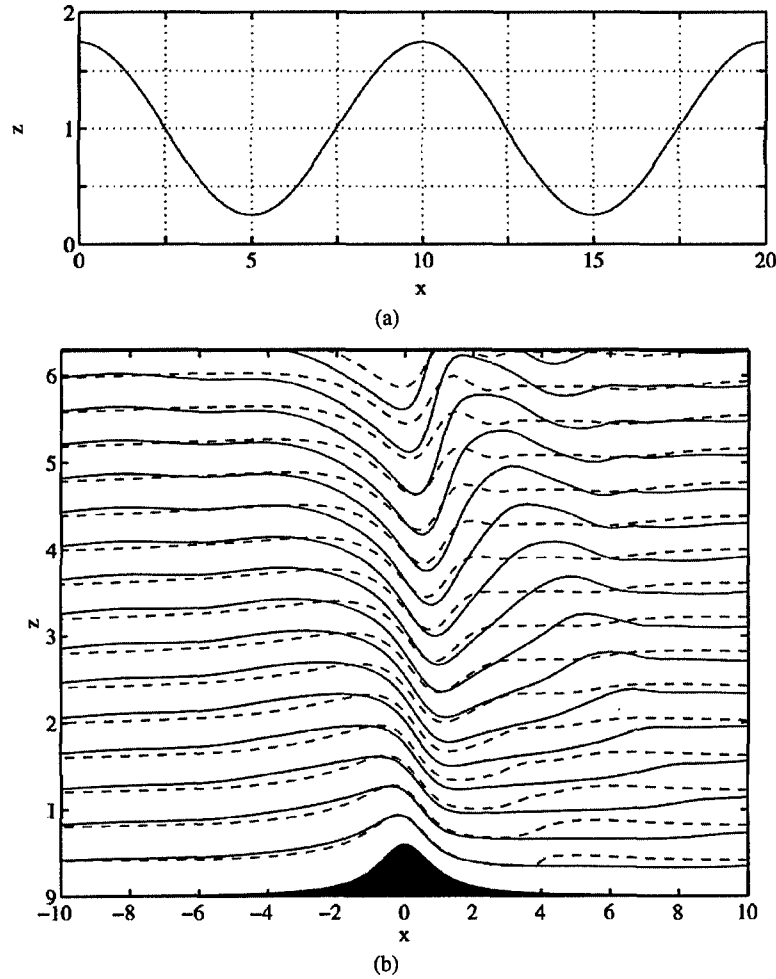


Fig. 20 Transients produced by monochromatic gradual temporal modulations in the free stream (a) background flow characterized by $t_a = 0.05\mu$, $\Delta = 0.75$ and $\omega_0 = 0.63$; (b) evolution of the response for $\varepsilon = 0.6$ and $\mu = 1/6$: dashed lines $t = 2.5$, solid lines $t = 12.5$. In this simulation, $\nu = 0.2$.

21. Skopovi, I.: A model for nonlinear gravity waves in stratified flows. Master's thesis, MIT (2002)
22. Skopovi, I.: The role of background flow variations in stratified flows over topography. Ph.D. thesis, MIT (2006)
23. Skopovi, I., Akylas, T.R.: The role of buoyancy-frequency oscillations in the generation of mountain gravity waves. Theor. Comput. Fluid Dyn. (in press)